Article

Space Charge Accumulation Characteristics in HVDC Cable under Temperature Gradient

Yifan Zhou *[ID]**, Wei Wang and Tailong Guo**

Beijing Key Laboratory of High Voltage & Electromagnetic Compatibility, North China Electric Power University, Beijing 102206, China; wwei@ncepu.edu.cn (W.W.); gtailong7@163.com (T.G.)
* Correspondence: yfzhou@ncepu.edu.cn

check for updates

Abstract: One of the main issues that affect the development of high-voltage direct-current (HVDC) cable insulation is the accumulation of space charge. The load operation of an HVDC cable leads to the formation of a radially distributed temperature gradient (TG) across the insulation. In this study, the space charge accumulation in a cross-linked polyethylene (XLPE) cable is measured under a DC electric field and TG using the pulsed electro-acoustic (PEA) method, and the effect of the TG on the space charge behavior is investigated. In addition, the bipolar charge transport (BCT) model and the conductivity model based on an improved cylindrical geometry are used to simulate the charge behavior in the HVDC XLPE cable under TG, and the experimental and simulated results are compared. The results show that the higher temperature of the cable conductor promotes the accumulation of homocharge near the side of high temperature. Additionally, with the increase of the TG, not only does more heterocharge accumulates adjacent to the side of low temperature, but more space charge also extends into the bulk of the cable insulation. More attention should be paid to the conductor shield layer and the insulation shield layer in HVDC cables. Moreover, the BCT model can more accurately describe the experimental results than the conductivity model.

Keywords: HVDC cable; space charge; pulsed electro-acoustic (PEA); temperature gradient (TG); cross-linked polyethylene (XLPE); conductivity model; bipolar charge transport (BCT) model

1. Introduction

High-voltage direct-current (HVDC) transmission technology is currently the mainstream technology used in the interconnection of regional grids and the long-distance and large-capacity transmission of power energy [1]. As the key power equipment in the construction of HVDC transmission systems, the HVDC cable has many advantages including high reliability, environmental friendliness, and visual concealment, and has become the preferred alternative to overhead transmission lines [2,3]. One of the main factors that limit the long-term advancement of polymer-insulated DC cables is the accumulation of charge, which is one of the significant reasons of insulation degradation [4,5]. Moreover, the charge accumulation can bring about the electric field distortion, accelerates the insulation aging, and can even cause insulation breakdown [6–8].

Rapid advances in HVDC transmission technology have led to higher requirements for the insulation performance of HVDC cables. Cross-linked polyethylene (XLPE) material has been extensively applied in HVDC cable insulation and has excellent chemical stability and dielectric properties. To restrain the charge accumulation and improve the polymer insulation performance of HVDC cables, it is inevitable to master the characteristics of charge. In addition, the action of the load current in the conductor leads to the heating of the cable core, thereby forming a radially distributed temperature gradient (TG) across the insulation. The behavior of charge in HVDC cables can be strongly influenced by the effect of the TG.

Among the numerous nondestructive measurement techniques, the pulsed electro-acoustic (PEA) method put forward by Takada has been extensively applicable for the space charge measurement [9]. The measurement results based on a film sample made of cable insulation cannot straight reveal the characteristics of charge accumulation in a coaxial cable. The cable insulation is related not only to the characteristics of the insulating material itself, but also to the geometric configuration of the coaxial cable. Due to the influence of cylindrical geometry, there is a nonuniformly distributed electric field. Moreover, the influence of the interface between the insulation and the electrodes cannot be neglected. Therefore, the behavior of charge in HVDC cable cannot be truly represented by an equivalent film sample, and only experimental measurement based on the coaxial cable can more accurately reflect the charge characteristics. To date, a few scholars have measured the distribution of space charge based on an HVDC cable under TG [10–15]. However, the effect of attenuation and dispersion causes the distortion of measurement waveform using the PEA method when acoustic waves travel in the coaxial cable. Simultaneously, the TG aggravates the effect of attenuation and dispersion on the propagation of acoustic waves. Therefore, the effect of the TG on the charge behavior can be clearly explained by the recovered measured waveform.

In addition, experimental measurement is limited by the measurement accuracy and spatial resolution of the device. The dynamic behavior, evolution regularity, and interaction mechanism of charges in an HVDC cable under TG must be further recognized. With the development of computer technology, numerical calculation has become a valid method by which to research the characteristics of charge in polymer insulation. There are typically two types of models on the description of the cable insulation properties, the first of which is the conductivity model, which has been served for the simulation of the distribution of the electric field and space charge in HVDC cables [16–20].

The second type of model is the microcosmic bipolar charge transport (BCT) model put forward by Alison et al. on the description of the behavior of space charge in XLPE material [21]. Le Roy et al. extended this model by introducing the process of charge detrapping via a detrapping coefficient to research the behavior of charge in low-density polyethylene (LDPE) material [22]. Based on this model, Wu et al. researched the behavior of charge in XLPE plaques under a TG [23]. These aforementioned numerical studies based on the BCT model revealed good consistency between the predicted and experimental results. Therefore, it has been proven that the model can effectively calculate the charge behavior in polymer insulating materials.

In most studies, the BCT model has been applied to flat specimens, and few studies have considered the influence of cylindrical geometry. Recently, the BCT model has been modified based on the cable geometry of HVDC cable insulation [24,25], but the diffusion motion of the charges in HVDC cable insulation has been neglected, and the diffusion coefficient is affected by the TG. In addition, the cylindrical geometry used for simulation is simplified and only considers the conductor and insulation layer; this simplification is different from the actual HVDC cable, and neglects the conductor shield layer and the insulation shield layer. Therefore, for comparison with experimental measurements, it is essential to select a more accurate model to calculate the behavior of charge in an HVDC XLPE cable under TG. However, little attention has been paid to the comparison between simulations by the conductivity model and BCT model.

In this paper, firstly based on the PEA experimental setup used for coaxial cables, the characteristics of charge accumulation in a XLPE cable under different TGs were measured and recovered. Then, the cylindrical geometry used for simulation was improved, and the diffusion motion of charges was added to the BCT model. The charge behavior in an HVDC cable under different TGs was simulated by both the BCT model and the conductivity model based on the improved cylindrical geometry, the simulation parameters used for the conductivity model were optimized based on the XLPE material. Finally, the investigation was performed on the effect of the TG on the charge behavior, and comparisons between the simulated and experimental results were discussed. This research provides a theoretical basis for the precise regulation of space charge accumulation in HVDC cables.

2. Simulation Methods

2.1. Improved Geometric Model

The modeling of the space charge in an HVDC cable should take into account the cylindrical geometry of the cable. The geometric configuration is illustrated in Figure 1, in which r_{in}, r_{out}, and r are respectively the inner radius of the cable insulation (line segment O–B), the outer radius of the cable insulation (line segment O–C), and the radius of the cable insulation.
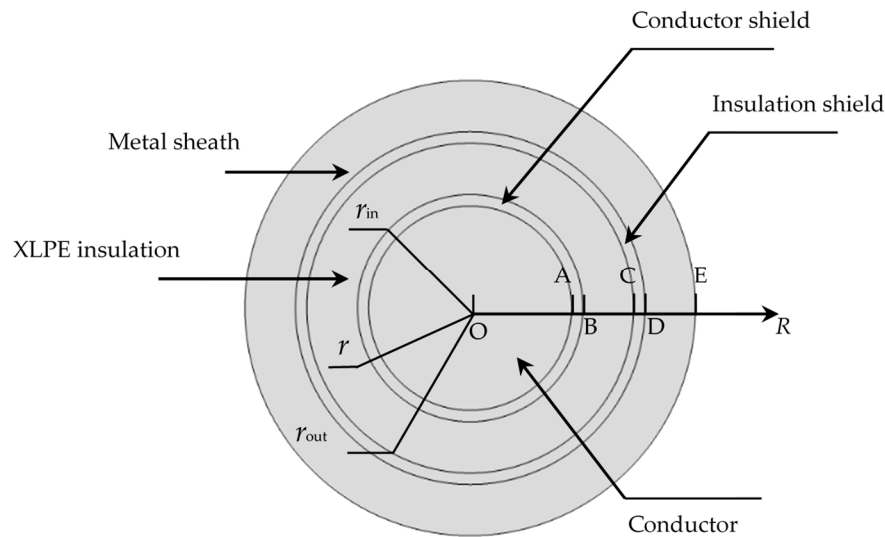

Figure 1. Geometric configuration.

The geometric configuration was employed for the simulation models. For the conductivity model, the two-dimensional circular configuration in Figure 1 was adopted to express the geometry of the cable cross-section. For the BCT model, a one-dimensional axisymmetric geometric model was constructed, and the geometric model presented in Figure 1 was established by 360° rotation of the radius O–E around the center O. From Figure 1, it demonstrates that the line segment B–C represents the radial line segment of the cable insulation, point B is the side with a high temperature (anode), and point C is the side with a low temperature (cathode). The behavior of charge in the cable insulation (line segment B–C) was investigated, and the material of the cable insulation was set to XLPE.

Moreover, due to the cylindrical geometry, the electric field and temperature are nonuniformly distributed in the HVDC cable insulation. The distribution of temperature is expressed as (1) [26].

$$T(r) \;=\; T_1 + \frac{(\ln r - \ln r_{in}) \cdot (T_2 - T_1)}{(\ln r_{out} - \ln r_{in})}, \tag{1}$$

where $T(r)$ denotes the temperature of the radius r, T_1 denotes the temperature of the radius r_{in}, and T_2 denotes the temperature of the radius r_{out}.

2.2. Conductivity Model

The expression in (2) is adopted to define the electric field and temperature dependency of conductivity [27]:

$$\sigma(E,T) \;=\; A \exp\left(\frac{-\varphi q}{k_B T}\right) \frac{\sinh(B|E|)}{|E|}, \tag{2}$$

where $\sigma(E,T)$ denotes the conductivity, q denotes the elementary charge, k_B denotes the Boltzmann constant, φ denotes the thermal activation energy, and A and B denote constants. Equation (2) originates from the hopping theory model of conduction in a dielectric material [27], and physically explains the E- and T-dependency of $\sigma(E,T)$.

The density of charge ρ is expressed by the theoretical expression (3) [17]:

$$\rho = -\frac{\varepsilon_0 \varepsilon_r}{\sigma} \frac{\partial \rho}{\partial t} + \vec{j} \cdot \nabla(\frac{\varepsilon_0 \varepsilon_r}{\sigma}), \tag{3}$$

where j represents the current density, ε_r represents the relative permittivity. Equation (3) indicates that if the current density j is not zero, the nonuniform ratio between the permittivity $\varepsilon_0 \varepsilon_r$ and the conductivity σ causes the charge ρ to accumulate.

2.3. BCT Model for Cylindrical Geometry

The BCT model describes the processes of the injection, transport, trapping, detrapping, and recombination of charge. In this model, the types of charge carriers include trapped holes, mobile electrons, mobile holes, and trapped electrons; the subscripts h and e respectively represent holes and electrons, B_e/B_h and D_e/D_h respectively represent the trapping and detrapping coefficients. Moreover, S_0, S_1, S_2, and S_3 respectively represent the recombination coefficients between the aforementioned charge carriers. Figure 2 presents the schematic representation of the mechanism of this model.
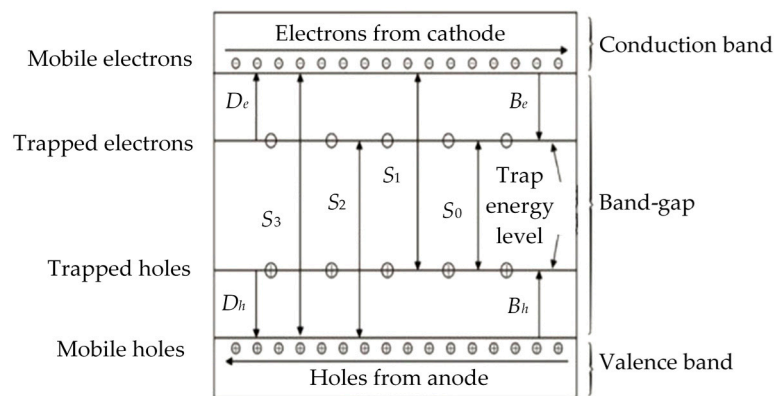

Figure 2. The mechanism of the bipolar charge transport (BCT) model [28].

The mechanism of this model illustrates that the generation of charge carriers originates from the injection at both electrodes, and the injected charge carriers move to the opposite electrodes under an electric field. Trap energy levels are localized in the band-gap, the capture of traps on the mobile charges results in the formation of trapped charges, and the distribution of a single trap energy level is applied to this model. The charges have a short trapping time in shallow traps, and shallow traps participate in the process of charge conduction, which can be represented by the mobility of E- and T-dependency [29]. The process of charge trapping (coefficients B_e and B_h) can be described by the distribution of a single trap energy level for charge carriers. By overcoming the barrier, the trapped charges can escape from deep traps, which can be described by the coefficients of detrapping D_e and D_h [28].

The charge injection is described by the Schottky law [28], as given by (4) and (5):

$$j_h(r_{in}, t) = AT^2(r) \exp\left(-\frac{\varphi_{ih}}{k_B T(r)}\right) \exp\left(\frac{e}{k_B T(r)} \sqrt{\frac{eE(r_{in}, t)}{4\pi \varepsilon_0 \varepsilon_r}}\right), \tag{4}$$

$$j_e(r_{out}, t) = AT^2(r) \exp\left(-\frac{\varphi_{ie}}{k_B T(r)}\right) \exp\left(\frac{e}{k_B T(r)} \sqrt{\frac{eE(r_{out}, t)}{4\pi \varepsilon_0 \varepsilon_r}}\right), \tag{5}$$

where $j_h(r_{in},t)$ and $j_e(r_{out},t)$ represent the holes' and electrons' injection current densities, and φ_{ih} and φ_{ie} are the holes' and electrons' injection barriers.

The charge transport is governed by (6)–(8) in cylindrical coordinates. Equation (6) is the continuity equation, Equation (7) is the transport equation, and Equation (8) is the Poisson equation.

$$\frac{\partial n_a(r,t)}{\partial t} + \frac{1}{r}\frac{\partial (j_a \cdot r)}{\partial r} = s_a(r,t), \tag{6}$$

$$j_a(r,t) = \mu_a(r,t) \cdot n_{a\mu}(r,t) \cdot E(r,t) - D_f\frac{dn_{a\mu}(r,t)}{dr}, \tag{7}$$

$$\frac{\partial^2 V(r,t)}{\partial r^2} + \frac{1}{r}\frac{\partial V(r,t)}{\partial r} = -\frac{\rho(r,t)}{\varepsilon_0\varepsilon_r}, \tag{8}$$

where n_a represents the charge carrier density; the subscript a represents the type of charge; $n_{h\mu}$ represents mobile holes; n_{ht} represents trapped holes; $n_{e\mu}$ represents mobile electrons; n_{et} represents trapped electrons; the subscripts t and μ respectively denote the trapped charge and mobile charge; j_a represents the conduction current density; $\mu_a(r,t)$ represents the mobility; V represents the applied voltage; $\rho(r,t)$ stands for the net charge density, which represents the sum of the four types of charge carriers; and D_f represents the diffusion coefficient, which indicates the diffusion movement of mobile charge carriers. The diffusion coefficient follows the Einstein relation, and the relationship between the diffusion coefficient, mobility, and temperature is expressed as (9).

$$D_f(r,t) = \mu_a(r,t).\frac{k_B T(r)}{e} \tag{9}$$

Charge transport between shallow traps is characterized by a hopping mechanism, by which electrons and holes move from site to site by overcoming a potential barrier [28]. Mobility as a function of the *E-* and *T*-dependency based on the hopping mechanism is defined by (10).

$$\mu_{e,h}(r,t) = \frac{2dv}{E(r,t)}\exp\left[\frac{ew_{\mu e,h}}{k_B T(r)}\right]\sinh\left[\frac{eE(r,t)d}{2k_B T(r)}\right], \tag{10}$$

where d represents the distance between traps, $w_{\mu e}$ and $w_{\mu h}$ represent the electrons' and holes' hopping barrier heights, and v represents the attempt to escape frequency and is defined as $v = k_B T(r)/h$, where h represents Planck's constant.

In (6), $s_a(r,t)$ represents the source term, and indicates the changes of local charge carriers density [30]. Moreover, S_0, S_1, S_2, and S_3 denote the recombination coefficients for n_{et}/n_{ht}, $n_{e\mu}/n_{ht}$, $n_{et}/n_{h\mu}$, and $n_{e\mu}/n_{h\mu}$, respectively. The changes of local charge carriers densities are described by (11)–(14).

$$s_{h\mu} = \frac{\partial n_{h\mu}}{\partial t} = D_h \cdot n_{ht} - S_2 \cdot n_{et} \cdot n_{h\mu} - B_h \cdot n_{h\mu} \cdot \left(1 - \frac{n_{ht}}{n_{oht}}\right) - S_3 \cdot n_{h\mu} \cdot n_{e\mu}, \tag{11}$$

$$s_{e\mu} = \frac{\partial n_{e\mu}}{\partial t} = D_e \cdot n_{et} - S_1 \cdot n_{ht} \cdot n_{e\mu} - B_e \cdot n_{e\mu} \cdot \left(1 - \frac{n_{et}}{n_{oet}}\right) - S_3 \cdot n_{h\mu} \cdot n_{e\mu}, \tag{12}$$

$$s_{ht} = \frac{\partial n_{ht}}{\partial t} = B_h \cdot n_{h\mu} \cdot \left(1 - \frac{n_{ht}}{n_{oht}}\right) - S_0 \cdot n_{ht} \cdot n_{et} - D_h \cdot n_{ht} - S_1 \cdot n_{ht} \cdot n_{e\mu}, \tag{13}$$

$$s_{et} = \frac{\partial n_{et}}{\partial t} = B_e \cdot n_{e\mu} \cdot \left(1 - \frac{n_{et}}{n_{oet}}\right) - S_0 \cdot n_{ht} \cdot n_{et} - D_e \cdot n_{et} - S_2 \cdot n_{h\mu} \cdot n_{et}, \tag{14}$$

where n_{oet} and n_{oht} respectively represent the electrons' and holes' trap densities. D_e and D_h are respectively defined by (15) and (16):

$$D_e(r,t) = v.\exp\left(\frac{-\psi_{et}}{k_B T(r)}\right), \tag{15}$$

$$D_h(r,t) \; = \; v.\exp\left(\frac{-\psi_{ht}}{k_B T(r)}\right), \tag{16}$$

where ψ_{et} and ψ_{ht} respectively represent the detrapping barrier heights for n_{et} and n_{ht}, and v represents the attempt to escape frequency.

3. Experimental Methods

3.1. Experimental Setup

Based on the principle of the PEA method, when a pulsed voltage superimposed on a DC voltage is applied to a cable core, the application of the pulsed electric stress causes the vibration of space charge and the modification of the electrostatic force distribution. Additionally, the acoustic waves' propagation in the cable sample is formed by the electrostatic force. Those acoustic waves then propagate toward the grounded electrode and are transformed into voltage signals by a piezoelectric sensor made with polyvinylidene fluoride (PVDF) attached to the ground electrode. The signals of output voltage are then amplified and observed by an oscilloscope.

An experimental setup was constructed, which included the PEA measurement system applied to the coaxial cable, an HVDC source, an HV pulse source, a transformer, and an anti-corona ball, oscilloscope, and computer, as shown in Figure 3. Anti-corona balls were placed at both ends of a measured cable to prevent corona discharge. To convert acoustic signals into electrical signals, a PVDF film was utilized for the piezoelectric sensor. A polymethyl methacrylate (PMMA) film was attached closely to the piezoelectric sensor to avoid the reflection of acoustic signals. A 64-dB gain amplifier was used to cause the amplification of output voltage signals. Fulfill data processing and correct the waveforms from the oscilloscope are implemented by the computer.
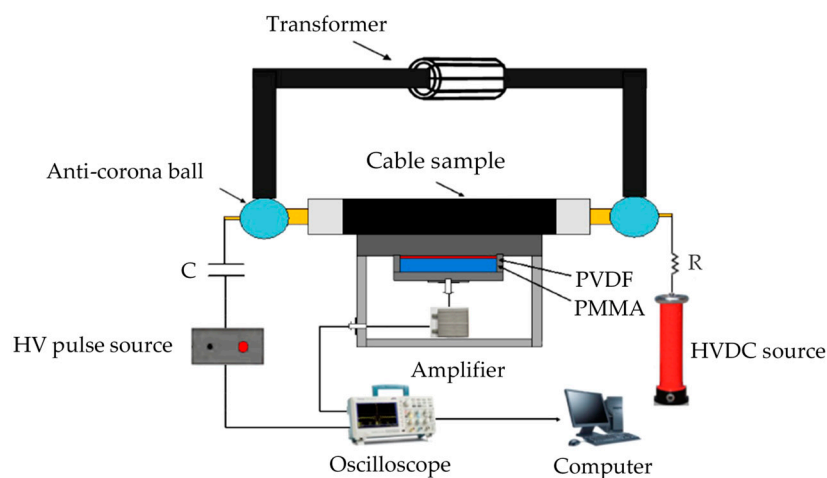

Figure 3. Schematic diagram of the experimental setup.

HVDC voltage was injected into the measured cable conductor by a current limiting resistor. The measurement system presented in Figure 3 adopted a flat ground electrode, which was directly in contact with the middle of the insulation shield layer. From Figure 3, an induced current was formed by an induction heating installation, which was made up of a voltage regulator, a transformer, an ammeter, and a current transformer. Another parallel XLPE cable without applied DC voltage and the measured cable were linked in an experimental closed loop. The cable core is heated by the induced current flowing in the experimental loop. The primary winding of the transformer was applied to the voltage regulator, and the connection cable passed through the transformer and served as the secondary winding. The induced current could be measured by the current transformer and an ammeter. By this means, the measured cable was heated as Joule heat generated by the action of the induced current, causing the temperature of the conductor to be higher than that of the insulation

shield layer. The other parallel XLPE cable was heated synchronously, the temperatures of the cable core and the insulation shield layer were detected by thermocouple sensors. The temperature of the cable core, as well as that of the insulation shield layer, could be regulated by the induction heating installation. Thus, a distribution of TG inside the insulation was generated before applying the DC voltage to the cable core.

The induced current heated the conductor for 1 h to ensure that the TG reached a steady state, after which a 67.5-kV DC voltage was applied to the conductor and the distribution of charge in the XLPE cable was measured. Table 1 reports the measured values of temperature of the conductor and the insulation shield layer.

Table 1. The relationship between the current, the temperature of the conductor, and the temperature of the insulation shield layer.

Symbol	Value	Value	Unit
Current	450	610	A
Temperature of conductor	55.3	86.8	°C
Temperature of insulation shield layer	40.2	57.1	°C

3.2. Experimental Results

The cable sample was selected as an actual single-core XLPE cable, the thickness of the insulation was 4.5 mm, and the material of the conductor was copper. The distribution of charge in the XLPE cable was measured under the DC voltage of 67.5 kV (the average electric field intensity was 15 kV/mm) and different TGs of 0, 3.3, and 6.6 °C/mm based on the experimental setup shown in Figure 3. From Figure 4a–c, the temperature differences formed by the TGs were respectively 0 °C (room temperature was 25 °C), 15 °C, and 30 °C. In Figure 4, t indicates the duration of the applied DC voltage, and ΔT and ∇T respectively represent the temperature difference and the steady TG. Considering the nonuniform distribution of electric field in the XLPE cable, the diffusion propagation of acoustic waves, the effect of attenuation and dispersion on the propagation of acoustic waves, and the effect of the TG, it was necessary to recover the measured waveforms. The experimental results presented in Figure 4 have therefore been corrected by the recovery algorithm developed in the authors' previous research [31].

In Figure 4, the thickness of 4.5 mm is the side of high temperature (anode), and the thickness of 0 mm is the side of low temperature (cathode). As shown in Figure 4a, there was no significant charge accumulation inside the insulation. Figure 4b,c indicate that when the steady TG values ∇T inside the cable insulation were 3.3 and 6.6 °C/mm (ΔT = 15 °C and 30 °C, respectively), heterocharge gradually accumulated near the side of low temperature, and homocharge gradually accumulated near the side of high temperature. Simultaneously, the accumulation of charge was gradually enhanced in the bulk of the cable insulation. At 5 h after the DC voltage was applied, the charge distribution extended greatly into the bulk, where the charge polarity was positive. In addition, by comparing Figure 4b,c, it is evident that the higher TG caused more heterocharge to accumulate adjacent to the low-temperature side.
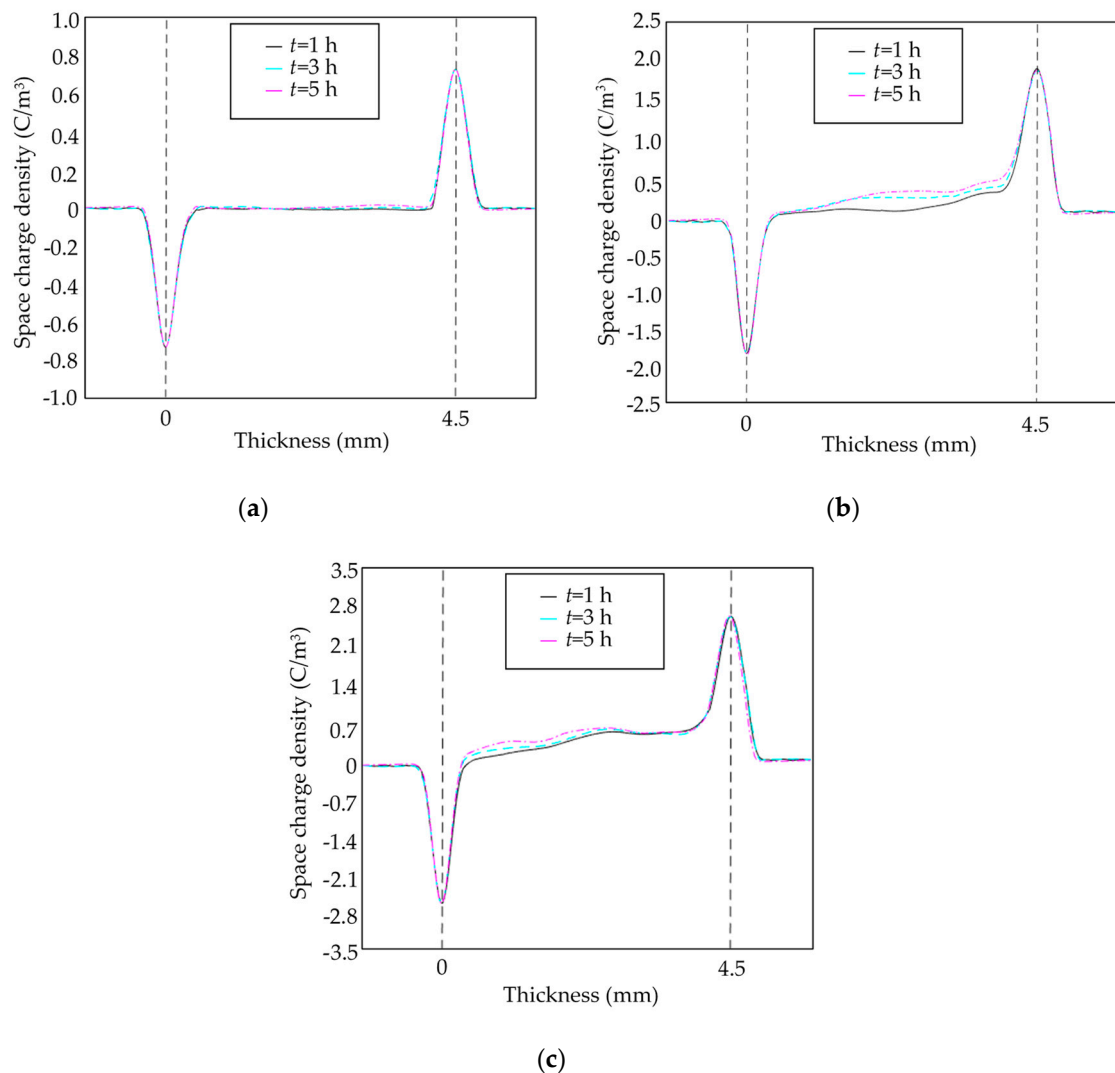
Figure 4. Space charge distribution under the applied DC voltage of 67.5 kV: (**a**) at room temperature; (**b**) insulation with a temperature difference of 15 °C; (**c**) insulation with a temperature difference of 30 °C.

4. Simulation Results

Based on the geometric configuration presented in Figure 1 and the mathematical principles for the conductivity model and BCT model, the behavior of charge in an XLPE cable under different TGs was described by the models, in which the insulation thickness of 4.5 mm was set to be equal to the thickness of the cable sample. It was necessary to ensure that the experiment and simulation could be conducted under the same electrical and thermal conditions, i.e., a 67.5-kV DC voltage was applied to the cable conductor in the simulation models, and the temperature differences were respectively set as 15 °C and 30 °C.

4.1. Simulation Results Based on the Conductivity Model

The flow chart for the determination of the density of charge based on the conductivity model is shown in Figure 5. The conductor, conductor shield layer, insulation shield layer, and metal sheath of the geometric model shown in Figure 1 were discretized using a uniform grid cell of thickness Δr. The insulation layer was meshed with a nonuniform grid cell of thickness Δr, and was set to be smaller closer to the conductor shield layer and the insulation shield layer to optimize the simulation results. The smallest size of the cell Δr was 800 nm.
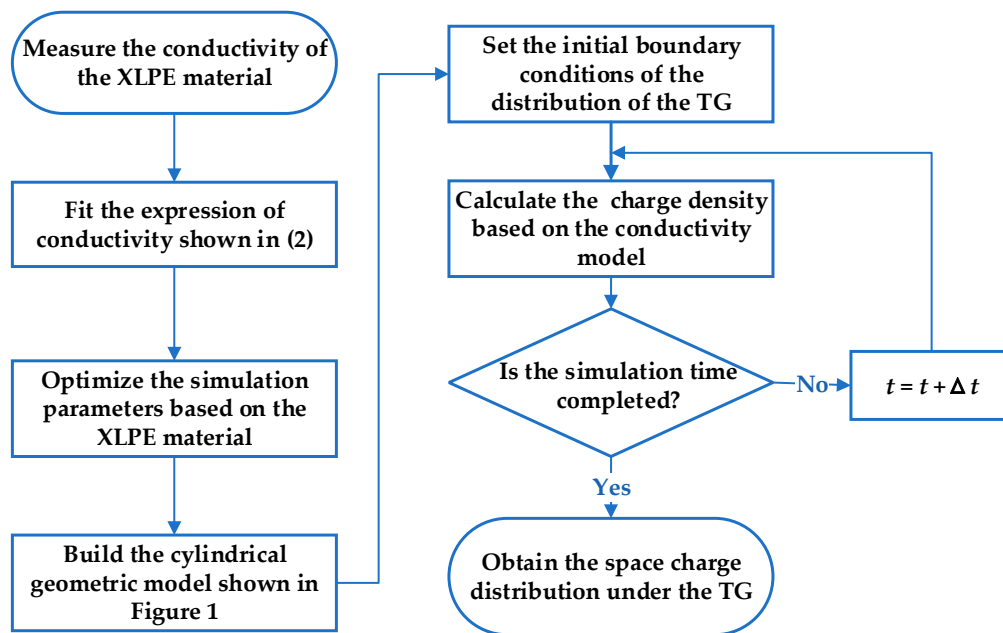
Figure 5. The flow chart of the simulation based on the conductivity model.

The simulation parameters require optimization based on the XLPE material, and the expression of conductivity given by (2) can be fitted by the experimental measurements of the conduction current. Therefore, the conductivity of the XLPE material was measured based on a measurement system shown in Figure 6, consisted of an HVDC source, a Keithley 6517B electrometer, a measurement system with a three-electrode structure, a temperature control system, and a computer. The current measurement resolution of the Keithley 6517B electrometer was set to 10^{-16} A. The three-electrode structure was composed of an HV electrode, a measuring electrode, and a guarding electrode, and the measuring electrode was connected to the electrometer. The shielding box was connected to the ground. The regulation of the voltage and temperature, as well as the collection of the conduction current, were controlled by the computer to complete the automatic measurement.
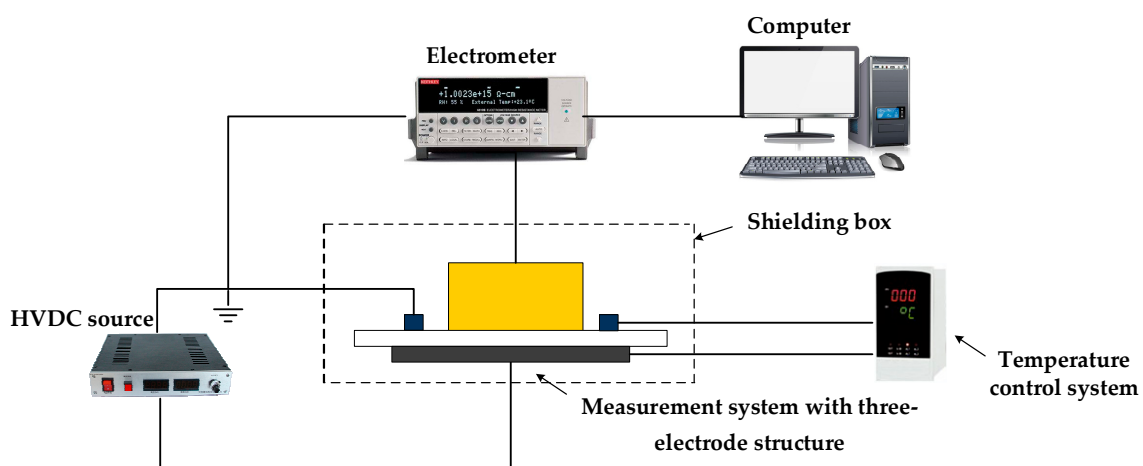

Figure 6. Schematic diagram of the measurement system.

In Figure 6, the diameter of the measuring electrode was 30 mm, and the test specimens were selected as XLPE films made of actual XLPE cable insulation, the thickness of which was 220 μm. At a certain temperature, the DC voltage applied to the XLPE test specimen was gradually increased, and the measured currents were respectively recorded when the duration of the applied DC voltage

was 20 min. Figure 7 presents the change of the conductivity of the XLPE sample with the electric field at 25 °C and 50 °C.
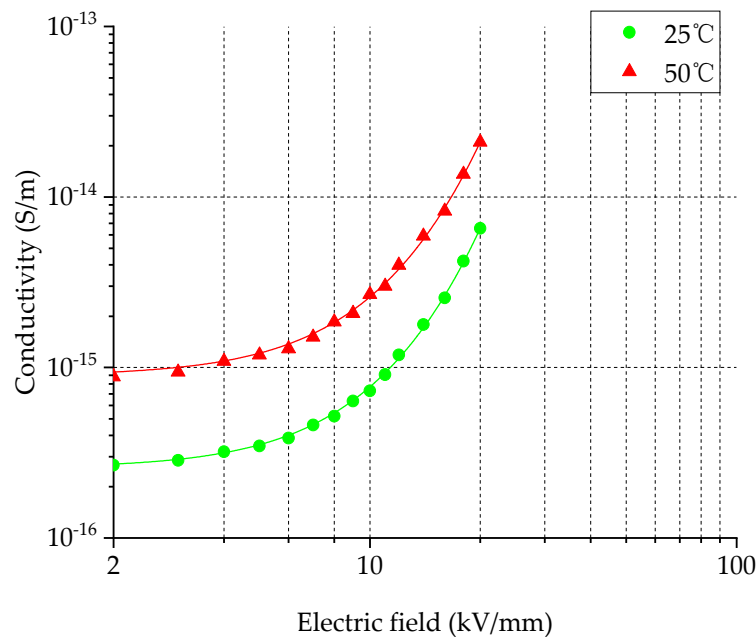

Figure 7. Change of the conductivity with the electric field at 25 °C and 50 °C.

The experimental data presented in Figure 7 were used for fitting (2) to obtain the parameters φ, A, and B, as reported in Table 2.

Table 2. Simulation parameters based on the conductivity model.

| Parameter	Value	Unit
A	3.18×10^7	$V/(\Omega \cdot m^2)$
B	1.65×10^{-7}	m/V
φ	0.89	eV

The simulation results at t = 5 h under the 67.5-kV DC voltage and different steady TGs are presented in Figure 8.

The conductor represents the high-temperature side, and the insulation shield layer represents the low-temperature side. Figure 8 reveals that at 5 h, the positive charges accumulated mainly near the cable conductor, the accumulation of negative charges appeared near the insulation shield layer, and the positive charges also accumulated in the bulk. Moreover, a comparison between Figure 8a,b was made, demonstrating that the increase of the temperature difference aggravated the accumulation of positive charges adjacent to the high-temperature side. Additionally, the charge near the cable conductor tended to gradually move toward the insulation shield layer, and the higher temperature difference caused more positive charges to accumulate in the bulk.

A one-dimensional truncation line was established in the insulation layer of the two-dimensional geometric model shown in Figure 1. Figure 9 presents the charge behavior under different steady TGs with the increase of time.

In both graphs in Figure 9, the thickness of 0 mm represents the high-temperature side, while the thickness of 4.5 mm represents the low-temperature side. It is evident that with the increase of time, the charge adjacent to the side of high temperature gradually moved toward the side of low temperature, and numerous positive charges appeared in the bulk, where the polarity was consistent with the applied DC voltage and the experimental results (Figure 4b,c). By comparing the simulation

results presented in Figure 9a,b, it is evident that the increase of the TG accelerated the accumulation of more positive charges in the bulk. These findings indicate that due to the function expression in (2), the magnitude of the conductivity gradient can be induced by the increase of the TG, which results in the accumulation of more positive charges in the bulk of the cable insulation.
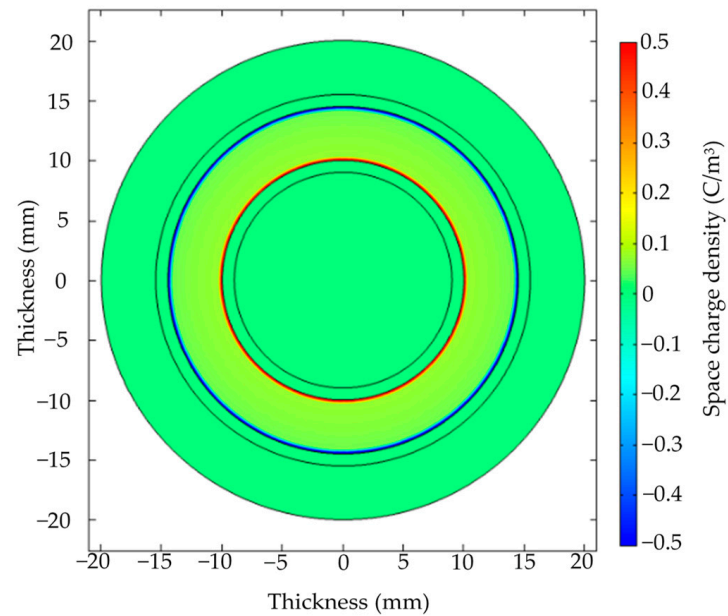
(**a**)
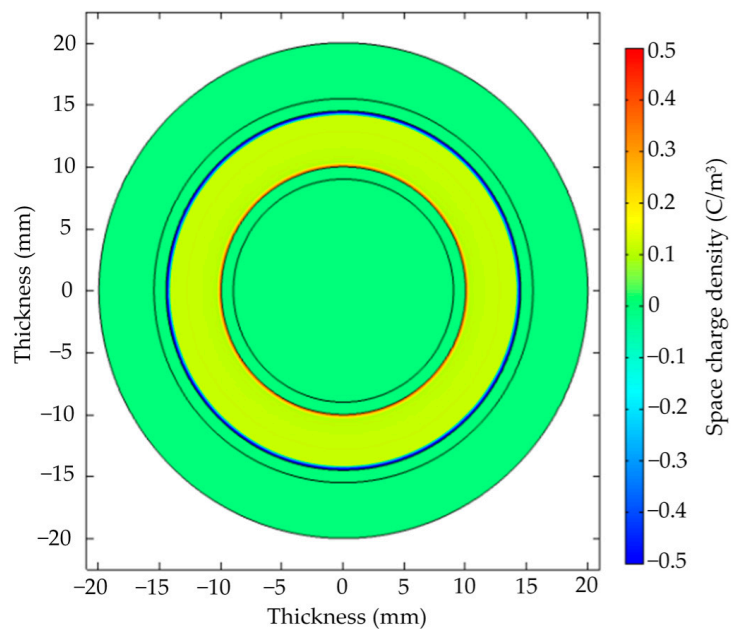
(**b**)

Figure 8. Simulation results at 5 h under the applied DC voltage of 67.5 kV: (**a**) insulation with the temperature difference of 15 °C; (**b**) insulation with the temperature difference of 30 °C.

(a)

(b)

Figure 9. Simulation results under the applied DC voltage of 67.5 kV: (**a**) insulation with the temperature difference of 15 °C; (**b**) insulation with the temperature difference of 30 °C.
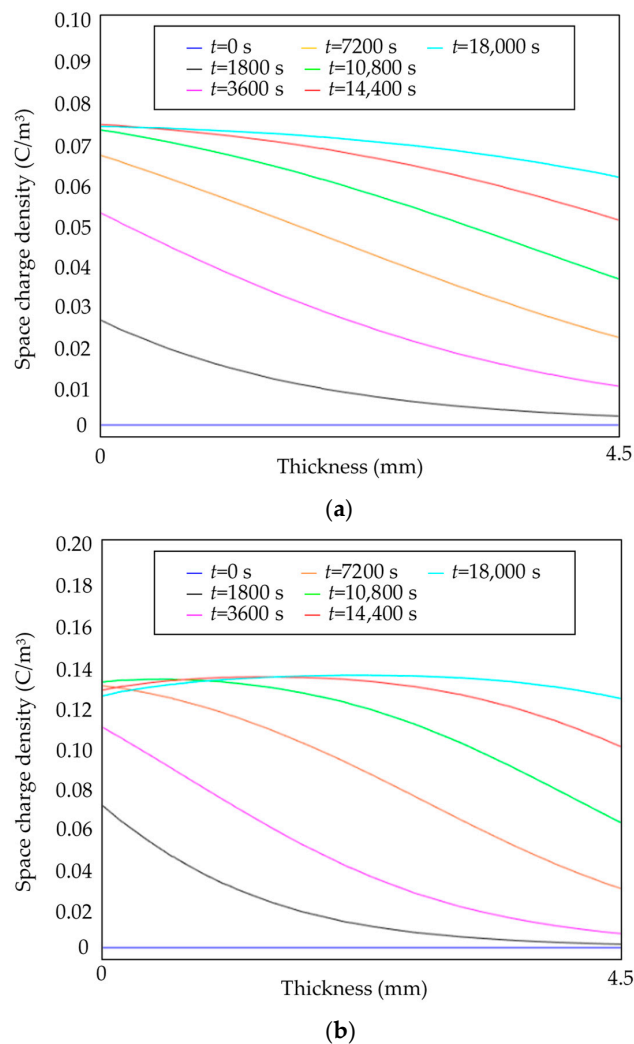
4.2. Simulation Results Based on the BCT Model

The BCT model was constructed based on the one-dimensional axisymmetric geometric model presented in Figure 1. To determine the density of space charge, each point at each time step, boundary conditions were established (4)–(5) and (6)–(8) were solved in combination with (9)–(13). The conductor, conductor shield layer, insulation shield layer, and metal sheath in the geometric model shown in Figure 1 were discretized using a uniform grid cell of thickness Δr. Additionally the insulation layer was meshed with a nonuniform grid cell of thickness Δr, which were set to be smaller closer to the conductor shield layer and the insulation shield layer to optimize the simulation results. The smallest cell size Δr was 800 nm, and the ratio of the size of maximal cell to the size of minimal cell was 100. The flow chart of the simulation based on the BCT model is presented in Figure 10.

The time step Δt used for the simulation computation satisfied the Courant-Friedrichs-Lewy (CFL) condition [32], demonstrating that the charge transport distance within each time step was less than the cell size. The CFL criterion is given by (17).

$$\Delta t < \frac{\Delta r}{\mu E},\tag{17}$$

where Δr is the cell size and μ is the mobility. The simulation parameters based on the XLPE insulation were selected based on guidance from existing research [22,24,33], as listed in Table 3.
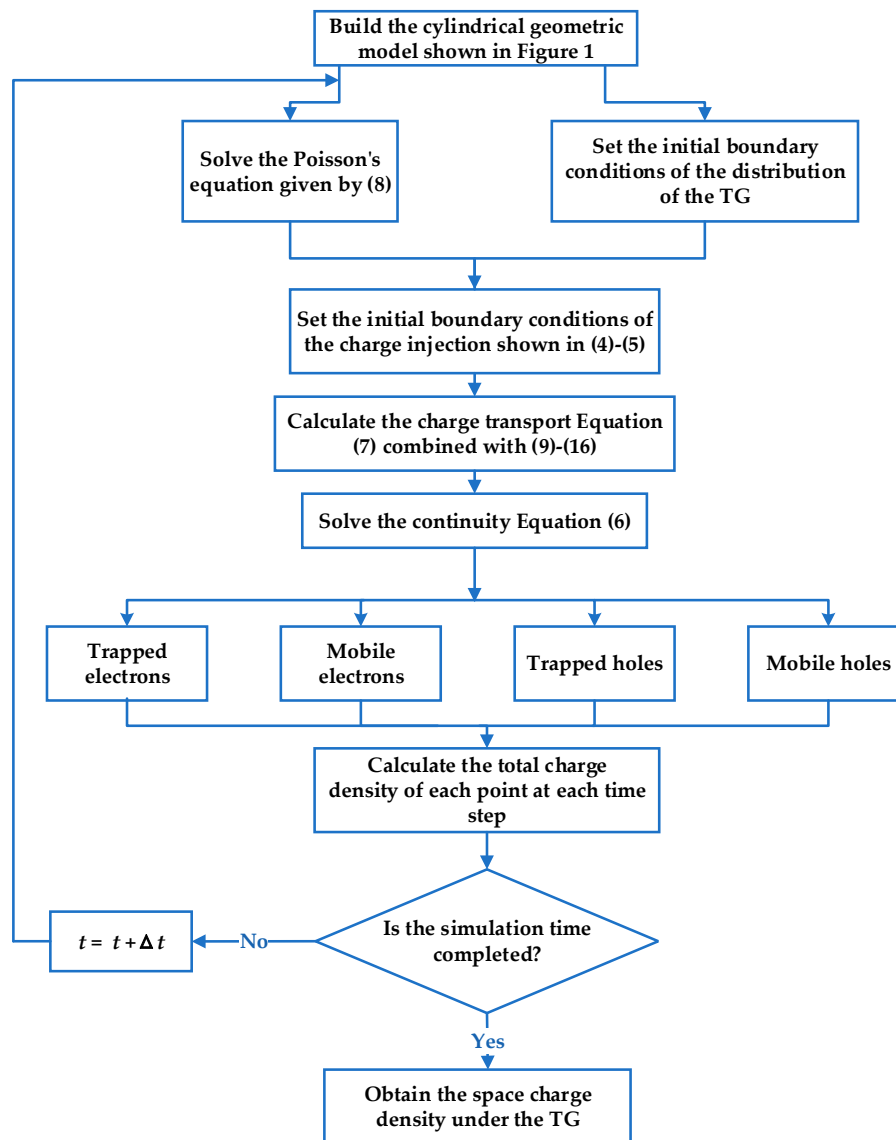
Build the cylindrical geometric model shown in Figure 1

Solve the Poisson's equation given by (8)

Set the initial boundary conditions of the distribution of the TG

Set the initial boundary conditions of the charge injection shown in (4)-(5)

Calculate the charge transport Equation (7) combined with (9)-(16)

Solve the continuity Equation (6)

Trapped electrons

Mobile electrons

Trapped holes

Mobile holes

Calculate the total charge density of each point at each time step

$t = t + \Delta t$ ← No ← Is the simulation time completed?

Yes

Obtain the space charge density under the TG

Figure 10. The flow chart of the simulation based on the BCT model.

Table 3. Simulation parameters based on the BCT model.

Symbol	Value	Unit
φ_{ih}	1.3	eV
φ_{ie}	1.27	eV
B_e	0.05	s^{-1}
B_h	0.05	s^{-1}
$w_{\mu e}$	0.71	eV
$w_{\mu h}$	0.65	eV
Ψ_{et}	0.9	eV
Ψ_{ht}	0.9	eV
n_{oet}	100	C/m^3
n_{oht}	100	C/m^3
S_0	4×10^{-3}	m^3/(C·s)
S_1	4×10^{-3}	m^3/(C·s)
S_2	4×10^{-3}	m^3/(C·s)
S_3	0	m^3/(C·s)

The simulation results under the applied DC voltage of 67.5 kV and different steady TGs with the increase of time are presented in Figure 11.
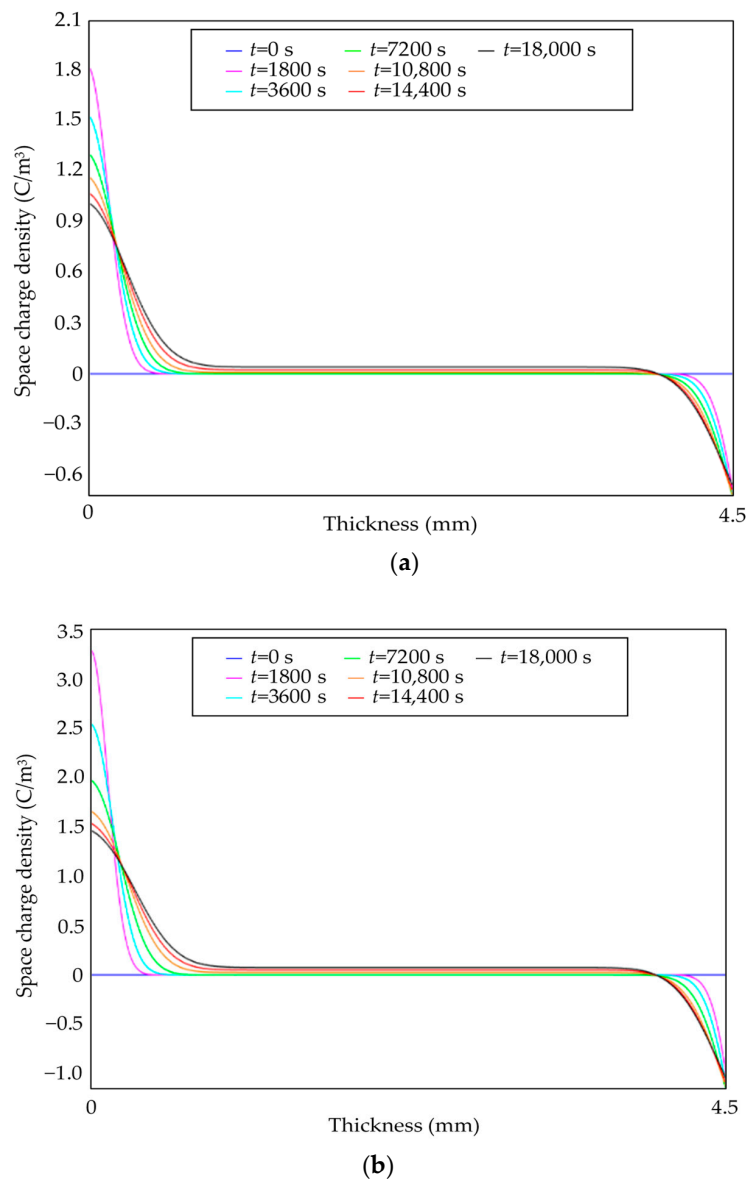

(**a**)

(**b**)

Figure 11. Simulation results under the applied DC voltage of 67.5 kV: (**a**) insulation with the temperature difference of 15 °C; (**b**) insulation with the temperature difference of 30 °C.

A comparison between Figure 11a,b was made, demonstrating that the amount of charge from the anode to cathode changed with the temperature difference. A higher temperature difference at both electrodes intensified the charge injection and promoted charge mobility. The holes injected from the anode became the dominant charges, which caused more holes to accumulate in the bulk. It can therefore be determined that a distinction between the injected holes and electrons was caused by the steady TG formed by the temperature difference at both electrodes; the higher temperature strengthened the injection of holes from the anode, and more holes tended to gradually move toward the cathode. Simultaneously, the higher TC enhanced the movement of the mobile charge carriers and the detrapping of the trapped charge carriers, and the concentration difference also weakened the recombination processes between the holes and electrons. As a result, numerous holes accumulated in the cable insulation, and the higher the TG, the more holes were accumulated in the bulk.

5. Comparison between Experimental and Simulated Results

In the models, it was assumed that the charge distribution was along the radial insulation. Comparison between the simulated and experimental results demonstrates that the simulated results can describe the space charge accumulation characteristics to some extent. However, there were some differences between the two simulation models.

By comparing the simulated results of the conductivity model (Figures 8 and 9) with the experimental results (Figure 4b,c) under the same cable insulation thickness and electrical and thermal conditions, it is clear that the process of charge movement was described by both results. It can also be observed the charge behavior in the XLPE cable was strongly influenced by the TG, i.e., more positive charges accumulated inside the cable insulation due to the higher TG. However, there remain some limitations of the conductivity model based on the cylindrical geometry. When the conductivity model in (2) was fitted by the experimental measurements of the conduction current, the mechanism of charge generation based on this macroscopic model was found to originate from the nonuniformity of the conduction current in the cable insulation. Simultaneously, the increase of TG influenced the conductivity gradient, which aggravated the accumulation of positive charges in the cable insulation. The simulated results based on this macroscopic model demonstrate the entire contribution of the different types of charges; however, there are distinctions in the behaviors of the respective types of charges during conduction, which are affected by different processes, such as charge generation and transport. Therefore, the mechanism of charge accumulation is more complex than that described by this macroscopic model.

By comparing the simulated results of the BCT model (Figure 11a,b) with the experimental results (Figure 4b,c) under the same cable insulation thickness and electrical and thermal conditions, it can be observed that both results described the injection of obvious charge at both electrodes, the movement of charge from the side with a high temperature to the side with a low temperature, and the accumulation of positive charges in the bulk. The microcosmic model can describe the experimental results more accurately, and effectively described the injection and the processes of transport (trapping, detrapping, and recombination). Although the simulated results were found to agree well with the experimental observations (i.e., the accumulation of homocharge near the side with a high temperature and positive charges in the bulk), there remain some limitations of the simulation of the accumulation of heterocharge near the side with a low temperature in the XLPE cable; the ionization process of impurities may therefore not be considered in this microcosmic model. In addition, some of the parameters used for this model were not optimized based on the XLPE material.

6. Conclusions

In this research, the characteristics of charge accumulation in a XLPE cable under different TGs were measured and recovered. Then, based on an improved cylindrical geometry, the BCT model and conductivity model were served for the simulation of the behavior of charge in an HVDC cable under different TGs. The simulation parameters in the conductivity model were optimized based on the XLPE material, and the diffusion motion of charges was added to the BCT model. Finally, the investigation was performed on the effect of the TG on the behavior of charge. Comparisons between the simulated and experimental results under the same cable insulation thickness and electrical and thermal conditions were made. The conclusions of this research are summarized as follows.

The experimental results can clearly demonstrate the characteristics of charge accumulation in a XLPE cable under different TGs. The results demonstrate that no significant charges accumulate in the insulation at room temperature, and under steady TG, heterocharge accumulates gradually near the side of low temperature, and homocharge accumulates gradually near the side of high temperature. The generation of homocharge adjacent to the side of high temperature can be promoted by the higher temperature at the conductor. With the increase of the TG, not only does more heterocharge accumulate adjacent to the side of low temperature, but more positive charges also extend greatly into the bulk of the cable insulation.

By comparing the simulated and experimental results, it is found that the behavior of charge in an HVDC cable can be described by both the conductivity model and BCT model to some extent, and the BCT model more accurately describes the experimental results. However, there remain some differences between the two simulation models. The simulation of heterocharge adjacent to the side of low temperature in the HVDC cable needs to be improved in the BCT model based on the cylindrical geometry, and some parameters used for this model must be optimized based on the XLPE material.

Therefore, more attention should be paid to the conductor shield layer and the insulation shield layer in HVDC cables. In future work, the electrical and thermal properties of the semi-conductive layer can be improved from the aspects of the doping of fillers, the processing technology, and the interface matching degree to evaluate the suppression effect of the space charge injection and accumulation, and to provide a theoretical basis for the precise regulation of space charge accumulation in HVDC cables.

Author Contributions: Conceptualization, Y.Z. and W.W.; methodology, Y.Z.; software, Y.Z.; investigation, Y.Z. and T.G.; writing—original draft preparation, Y.Z.; writing—review and editing, Y.Z. and W.W.; supervision, W.W. All authors have read and agreed to the published version of the manuscript.

References

1. Mazzanti, G.; Marzinotto, M. *Extruded Cables for High-Voltage Direct-Current Transmission: Advances in Research and Development*; John Wiley & Sons: Hoboken, NJ, USA, 2013.
2. Fabiani, D.; Montanari, G.C.; Laurent, C.; Teyssedre, G.; Morshuis, P.H.F.; Bodega, R.; Dissado, L.A.; Campus, A.; Nilsson, U.H. Polymeric HVDC cable design and space charge accumulation. Part 1: Insulation/semicon interface. *IEEE Electr. Insul. Mag.* **2007**, *23*, 11–19. [CrossRef]
3. Li, Z.; Du, B. Polymeric insulation for high-voltage DC extruded cables: Challenges and development directions. *IEEE Electr. Insul. Mag.* **2018**, *34*, 30–43. [CrossRef]
4. Dissado, L.A.; Fothergill, J.C. *Electrical Degradation and Breakdown in Polymers*; Peter Peregrinus: London, UK, 1992.
5. Montanari, G.C. Bringing an insulation to failure: The role of space charge. *IEEE Trans. Dielectr. Electr. Insul.* **2011**, *18*, 339–364. [CrossRef]
6. Zhang, Y.; Lewiner, J.; Alquie, C.; Hampton, N. Evidence of strong correlation between space-charge buildup and breakdown in cable insulation. *IEEE Trans. Dielectr. Electr. Insul.* **1996**, *3*, 778–783. [CrossRef]
7. Dissado, L.A.; Mazzanti, G.; Montanari, G.C. The role of trapped space charges in the electrical aging of insulating materials. *IEEE Trans. Dielectr. Electr. Insul.* **1997**, *4*, 496–506. [CrossRef]
8. Mazzanti, G.; Montanari, G.C.; Dissado, L.A. Electrical aging and life models: The role of space charge. *IEEE Trans. Dielectr. Electr. Insul.* **2005**, *12*, 876–890. [CrossRef]
9. Li, Y.; Yasuda, M.; Takada, T. Pulsed electroacoustic method for measurement of charge accumulation in solid dielectrics. *IEEE Trans. Dielectr. Electr. Insul.* **1994**, *1*, 188–195.
10. Liu, R.; Takada, T.; Takasu, N. Pulsed electroacoustic method for measurement of charge distribution in power cables under both dc and ac electric fields. *J. Phys. D Appl. Phys.* **1993**, *26*, 986–993. [CrossRef]
11. Bodega, R. Space Charge Accumulation in Polymeric High Voltage DC Cable Systems. Ph.D. Thesis, Delft University of Technology, Delft, The Netherlands, 2006.
12. Delpino, S.; Fabiani, D.; Montanari, G.C.; Laurent, C.; Teyssedre, G.; Morshuis, P.H.F.; Bodega, R.; Dissado, L.A. Polymeric HVDC cable design and space charge accumulation. Part 2: Insulation interfaces. *IEEE Electr. Insul. Mag.* **2008**, *24*, 14–24. [CrossRef]
13. Fu, M.; Dissado, L.A.; Chen, G.; Fothergill, J.C. Space charge formation and its modified electric field under applied voltage reversal and temperature gradient in XLPE cable. *IEEE Trans. Dielectr. Electr. Insul.* **2008**, *15*, 851–860. [CrossRef]
14. Choo, W.; Chen, G.; Swingler, S.G. Electric field in polymeric cable due to space charge accumulation under DC and temperature gradient. *IEEE Trans. Dielectr. Electr. Insul.* **2011**, *18*, 596–606. [CrossRef]
15. Chen, C.; Bu, Y.; Wang, X.; Cheng, C.H.; Wu, K. A comparison of space charge behaviors in coaxial cable and film sample under temperature gradient. *IEEE Trans. Dielectr. Electr. Insul.* **2019**, *26*, 1941–1948.

16. Jeroense, M.J.P.; Morshuis, P.H.F. Electric fields in HVDC paper-insulated cables. *IEEE Trans. Dielectr. Electr. Insul.* **1998**, *5*, 225–236. [CrossRef]

17. Morshuis, P.H.F.; Bodega, R.; Fabiani, D.; Montanari, G.C.; Dissad, L.A.; Smituthor, J.J. Calculation and measurement of space charge in MV-size extruded cables systems under load conditions. In Proceedings of the 2007 IEEE International Conference on Solid Dielectrics, Winchester, UK, 8–13 July 2007; pp. 502–505.

18. Vu, T.T.N.; Teyssedre, G.; Vissouvanadin, B.; Le Roy, S.; Laurent, C. Correlating conductivity and space charge measurements in multi-dielectrics under various electrical and thermal stresses. *IEEE Trans. Dielectr. Electr. Insul.* **2015**, *22*, 117–127. [CrossRef]

19. Liu, Y.; Zhang, S.; Cao, X.; Zhang, C.; Li, W. Simulation of electric field distribution in the XLPE insulation of a 320 kV DC cable under steady and time-varying states. *IEEE Trans. Dielectr. Electr. Insul.* **2018**, *25*, 954–964. [CrossRef]

20. Jörgens, C.; Clemens, M. Electric field model at interfaces in high voltage cable systems. In Proceedings of the 2019 19th International Symposium on Electromagnetic Fields in Mechatronics, Nancy, France, 29–31 August 2019; pp. 1–3.

21. Alison, J.M.; Hill, R.M. A model for bipolar charge transport, trapping and recombination in degassed crosslinked polyethene. *J. Phys. D Appl. Phys.* **1994**, *27*, 1291–1299. [CrossRef]

22. Le Roy, S.; Teyssedre, G.; Laurent, G. Charge transport and dissipative processes in insulating polymers: Experiments and model. *IEEE Trans. Dielectr. Electr. Insul.* **2005**, *12*, 644–654. [CrossRef]

23. Lv, Z.P.; Cao, J.Z.; Wang, X.; Wang, H.T.; Wu, K.; Dissado, L.A. Mechanism of space charge formation in cross linked polyethylene (XLPE) under temperature gradient. *IEEE Trans. Dielectr. Electr. Insul.* **2015**, *22*, 3186–3196. [CrossRef]

24. Le Roy, S.; Teyssedre, G.; Laurent, C. Modelling space charge in a cable geometry. *IEEE Trans. Dielectr. Electr. Insul.* **2016**, *23*, 2361–2367. [CrossRef]

25. Zhan, Y.; Chen, G.; Hao, M. Space charge modelling in HVDC extruded cable insulation. *IEEE Trans. Dielectr. Electr. Insul.* **2019**, *26*, 43–50. [CrossRef]

26. Fabiani, D.; Montanari, G.C.; Laurent, C.; Teyssedre, G.; Morshuis, P.H.F.; Bodega, R.; Dissado, L.A. HVDC cable design and space charge accumulation. Part 3: Effect of temperature gradient. *IEEE Electr. Insul. Mag.* **2008**, *24*, 5–14. [CrossRef]

27. Boggs, S.; Damon, D.H.; Hjerrild, J.; Holboll, J.T.; Henriksen, M. Effect of insulation properties on the field grading of solid dielectric DC cable. *IEEE Trans. Power Deliv.* **2001**, *16*, 456–461. [CrossRef]

28. Boufayed, F.; Teyssedre, G.; Laurent, C.; Le Roy, S. Models of bipolar charge transport in polyethylene. *J. Phys. D Appl. Phys.* **2006**, *100*, 104105. [CrossRef]

29. Teyssedre, G.; Laurent, C. Charge transport modeling in insulating polymers: From molecular to macroscopic scale. *IEEE Trans. Dielectr. Electr. Insul.* **2005**, *12*, 857–875. [CrossRef]

30. Baudoin, F.; Le Roy, S.; Teyssedre, G.; Laurent, C. Bipolar charge transport model with trapping and recombination an analysis of the current versus applied electric field characteristic in steady state conditions. *J. Phys. D Appl. Phys.* **2007**, *41*, 025306. [CrossRef]

31. Wang, W.; He, D.; Chen, S. Correction of acoustic wave in PEA space charge measurement on cable under temperature gradient. *High Volt. Eng.* **2015**, *41*, 1084–1089.

32. Le Roy, S. Numerical methods in the simulation of charge transport in solid dielectrics. *IEEE Trans. Dielectr. Electr. Insul.* **2006**, *13*, 239–246. [CrossRef]

33. Lan, L. Effect of Temperature on Space Charge Distribution in Polymer Insulation. Ph.D. Thesis, Shanghai Jiao Tong University, Shanghai, China, 2015.

Publisher's Note: MDPI stays neutral with regard to jurisdictional claims in published maps and institutional affiliations.